

## Surface and subsurface damages in nanoindentation tests of compound semiconductor InP

This content has been downloaded from IOPscience. Please scroll down to see the full text.

2008 J. Micromech. Microeng. 18 105018

(<http://iopscience.iop.org/0960-1317/18/10/105018>)

[View the table of contents for this issue](#), or go to the [journal homepage](#) for more

Download details:

IP Address: 131.113.58.246

This content was downloaded on 26/06/2015 at 09:23

Please note that [terms and conditions apply](#).

# Surface and subsurface damages in nanoindentation tests of compound semiconductor InP

Jiwang Yan<sup>1</sup>, Jun'ichi Tamaki<sup>2</sup>, Hongwei Zhao<sup>3</sup>  
and Tsunemoto Kuriyagawa<sup>1</sup>

<sup>1</sup> Department of Nanomechanics, Tohoku University, Aramaki Aoba 6-6-01, Aoba-ku, Sendai 980-8579, Japan

<sup>2</sup> Department of Mechanical Engineering, Kitami Institute of Technology, Koen-cho 165, Kitami, Hokkaido 090-8507, Japan

<sup>3</sup> School of Mechanical Science and Engineering, Nanling Campus, Jilin University, Changchun, Jilin 130025, People's Republic of China

E-mail: [yanjw@pm.mech.tohoku.ac.jp](mailto:yanjw@pm.mech.tohoku.ac.jp)

Received 10 June 2008, in final form 29 August 2008

Published 19 September 2008

Online at [stacks.iop.org/JMM/18/105018](http://stacks.iop.org/JMM/18/105018)

## Abstract

Nanoindentation tests were conducted on single-crystal indium phosphide (InP) using a Vickers indenter and a spherical indenter over a wide load range. The resulting indents were examined using scanning electron microscopy, cross-sectional transmission electron microscopy and selected area diffraction. Effects of the indenter type and indentation load on the surface cracking behavior, load–displacement characteristics and subsurface damage were investigated. The results showed that the cracking behavior and critical load for crack generation depends strongly on the indenter geometry and orientation. Pop-in events occur during loading in the case of the spherical indenter, but not in the case of the Vickers indenter. It was demonstrated that dislocations dominate the deformation mechanism, and no phase transformation occurs. The indenter contact immediately causes a high-density dislocation region, below which extend slip bands. The stress field of the indented zone was simulated by the finite element method, and the stress concentration regions corresponded to the high-density dislocation regions.

(Some figures in this article are in colour only in the electronic version)

## 1. Introduction

Single crystalline indium phosphide (InP) is an emerging compound semiconductor material for high-performance optoelectronic communication components, such as light-sensitive sensor elements, optical integrated circuits and laser diode elements. The fabrication of InP substrates involves a series of precision material removal processes, such as cutting, slicing, grinding, lapping and polishing. Most of the conventional manufacturing processes of InP follow those of silicon, which are well established. However, owing to distinct differences in material properties, the optimum machining conditions for silicon may not be suitable for InP. Therefore, it is important to investigate the micromechanical

properties, deformation and fracture mechanisms, and precision machining characteristics of InP at the micro/nano level to optimize the wafer fabrication processes.

Indentation is an effective method for characterizing the mechanical properties and machinability of a material. There is an abundance of literature on micro- and nanoindentation of silicon [1–10], which has contributed significantly to the understanding of the silicon machining process and innovations in the manufacturing technology of silicon wafers. In comparison, the literature on nanoindentation of InP is very limited. In the early 1970s, Brasen [11] investigated the hardness anisotropy of InP with a Knoop indenter at a fixed load of 50 g (0.49 mN). Bourhis *et al* [12] investigated the material flow of InP below a Vickers indenter at a high

temperature ( $400^{\circ}\text{C}$ ) and a fixed load of 1 N, and demonstrated the material's plasticity at high temperature. Yonenaga and Suzuki [13] investigated the temperature dependence of hardness for many semiconductor materials including InP at a fixed maximum load of 0.5 N, and confirmed the decrease in hardness with increasing temperature. Most of these studies were conducted under a high load (0.5 N or higher), and thus can be categorized as 'microindentation' tests. As recent 'nanoindentation' tests, Bradby *et al* [14–16] investigated the discontinuities in load–displacement curves (i.e., 'pop-in' events), subsurface dislocations and cracking behavior of gallium arsenide (GaAs) and InP at a load below 50 mN using a spherical indenter with a tip radius of  $4.2\ \mu\text{m}$ .

These studies have revealed some important aspects of InP deformation due to mechanical contacts, and the experimental data are also very useful for understanding the machining process. However, to date, there have been no experimental investigations into the effects of indenter geometry on the deformation/fracture of InP. In particular, its response to an extremely sharp indenter under an extremely small load at room temperature has not yet been determined, although these experimental conditions are geometrically and energetically akin to those of ultraprecision machining [17, 18]. Moreover, there is still no literature on the threshold values of indentation depth and load for crack generation in InP, which are important process criteria for conducting ductile-regime machining.

In this paper, we carried out nanoindentation tests on InP to examine the fundamental deformation/fracture behavior and ultraprecision machinability. We used an extremely sharpened Vickers indenter to simulate a sharp diamond cutting tool or an ultrafine abrasive grain, and a spherical indenter to simulate a dull cutting tool or a coarse abrasive grain, respectively. We investigated the load effects on surface microfractures and found the boundary conditions to achieve a ductile response at room temperature for each indenter type. The subsurface damage caused by indentation was examined by cross-sectional observations and finite element method (FEM) simulations. It is expected that the results of this paper will help in determining process parameters for low-damage ductile machining of InP substrates.

## 2. Experimental details

### 2.1. Indentation tests

Nanoindentation experiments were carried out on an ENT-1100a model nanoindentation system, produced by Elionix Corp., Japan. The indenter has a loading resolution of 0.01 mN, and a depth sensing resolution of 0.3 nm. The indenter shape is known to have a strong effect on the indentation behavior of materials. To simulate machining processes using different tool geometries, two types of indenters were used: a sharp pyramid-type indenter, namely, a Vickers indenter, and a spherical indenter. Figure 1 shows scanning electron microscope (SEM) micrographs of the Vickers indenter and spherical indenter. Both indenters are made of single-crystalline diamond. The spherical indenter has a nominal tip radius of  $10\ \mu\text{m}$ . The Vickers indenter

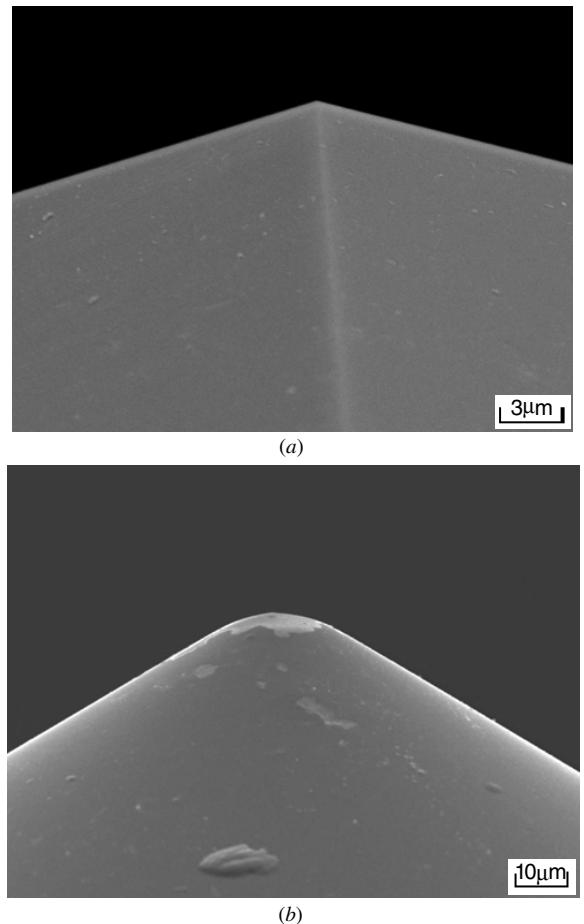


**Figure 1.** SEM micrographs of the indenter tips: (a) Vickers indenter and (b) spherical indenter.

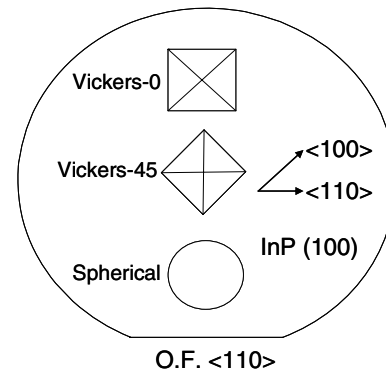


**Figure 2.** Schematic of indenter orientations with respect to the specimen.

has a face angle of  $68^{\circ}$ . In order to examine the effects of indenter face/ridge orientation on material deformation, the Vickers indenter was oriented in two ways: one face of the indenter was either parallel (Vickers-0) or  $45^{\circ}$  (Vickers-45) to the orientation flat (OF) of the wafer, as shown in figure 2.

In nanoindentation tests at an extremely small load, the penetration depth of the indenter into the specimen material is also extremely small, and thus, the influence of the indenter tip radius becomes significant. To be able to treat the Vickers indenter as a 'sharp' indenter, the tip radius must be as small as

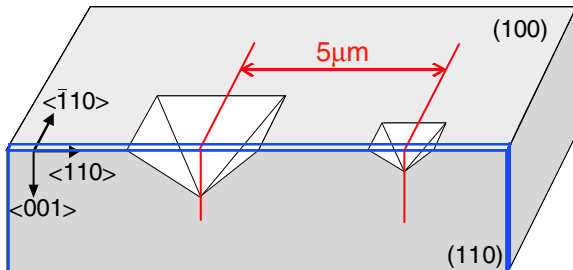


**Figure 3.** Schematic showing the position of the TEM sample prepared for cross-sectional observation.

possible because a blunt Vickers indenter would be equivalent to a ‘spherical’ indenter. Previous studies have not taken this into account. In the present study, to confirm the tip radius, we measured the indenter tip with a special SEM unit with two electron detectors. The tip radius was estimated to be smaller than 20 nm, which is comparable to that of an extremely sharpened diamond cutting tool.

The specimen is a device-grade semi-insulating single-crystal InP wafer produced by the liquid encapsulation Czochralski (LEC) method. The wafer was doped with Fe at a doping level of  $\leq 2.0 \times 10^{17}$  atoms  $\text{cm}^{-3}$ . The electrical resistivity is  $\geq 1 \times 10^6 \Omega \text{ cm}$ . The wafer is 50 mm in diameter, 0.45 mm in thickness and has a mirror-polished finish. The wafer has a (100) surface plane orientation and an orientation flat in the  $\langle 110 \rangle$  direction. The maximum load was varied from 10 to 1000 mN. The loading and unloading times were both fixed to 5 s. Thus, the loading/unloading rate varied between 2 and 200  $\text{mN s}^{-1}$ . The holding time at maximum load was 1 s. At each load, ten indentations were made, the pitch between which was set to 100  $\mu\text{m}$ . All indentations were made at ambient pressure and room temperature.

## 2.2. Indent observation

All indents were observed by SEM to examine the shape of the indent and check if there was any fracture damage. To prepare a transmission electron microscope (TEM) sample containing multiple indentations, a few indentations were specially made at a pitch of 5  $\mu\text{m}$ . At this small pitch, interaction phenomena might be observed between neighboring indentations. The indentations were then cut out from the wafer along the indenter centre (see figure 3) and thinned to below 100 nm by a focused ion beam (FIB) for the cross-sectional TEM observation. To protect the sample from damage during FIB processing, a thin layer of platinum/palladium (Pt–Pd) and carbon (total thickness  $\approx 0.5 \mu\text{m}$ ) was deposited over the surface. The TEM (Hitachi High-Technologies H-8000) was operated at an accelerating voltage of 200 kV.

## 2.3. Finite element analysis

The elastic–plastic finite element method (FEM) was used to analyze the stress field beneath the indentations, and the results were linked to the TEM results of subsurface

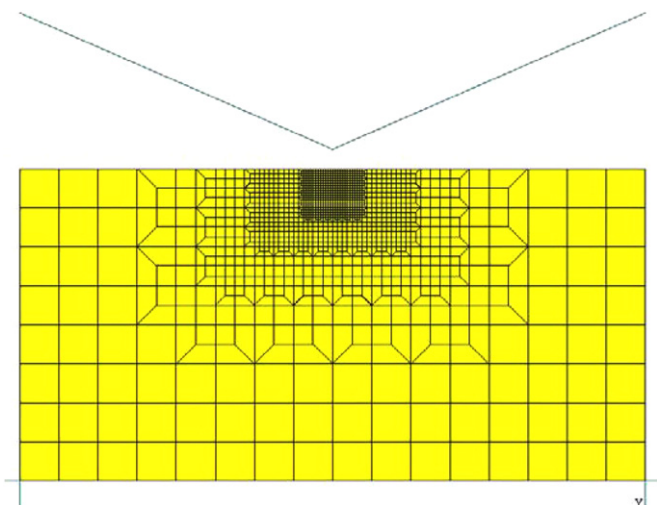


**Figure 4.** FEM simulation model for nanoindentation with a Vickers indenter.

damage. The stress-field analysis was carried out using the commercial nonlinear finite element program MSC-Marc, which enables studying large permanent deformations and part-to-part contact problems. The program was operated by combining with a pre/post-processor, Mentat. The indenter tip was modeled as a rigid conical tool and the InP material was modeled as an elastic–plastic body. The piecewise linear constitutive work-flow stress model was used to characterize the strain–stress relationship in the deformation of InP. The simulation model of the Vickers indentation is shown in figure 4.

The simulation was conducted on the InP (100) plane with isotropic elastic–plastic properties. The thickness of the workpiece is 800 nm and the width is 1600 nm. Rigid walls were used as the boundaries of the workpiece. The workpiece is constructed by 1392 bilinear quadrilateral elements. Elements were automatically remeshed during indentation based on an adaptive remeshing criterion involving three parameters: strain change, element distortion and penetration. Young’s modulus of the workpiece was set to 101 GPa and Poisson’s ratio was 0.29.

Elastic/plastic deformation in indentation is also influenced by friction between the indenter and specimen material. While the friction coefficient between diamond and InP remains unknown, with no literature available on the issue, we simply assume that it is on the same order as that between diamond and diamond. For diamond-on-diamond contact, the dynamic friction coefficient stabilizes at a value of 0.05–0.08 after surface polishing [19]. The friction coefficient of crystalline diamond on CVD diamond coatings ranges from 0.5 for rough styluses on rough coatings ( $R_a > 200 \text{ nm}$ ) to 0.03 for smooth styluses on smooth coatings ( $R_a \approx 1 \text{ nm}$ ) [20]. In the present study, since both the indenter surface and the specimen surface have been precisely polished to be very smooth, we assumed the friction coefficient between the indenter and the specimen to be 0.05 in the FEM simulation.

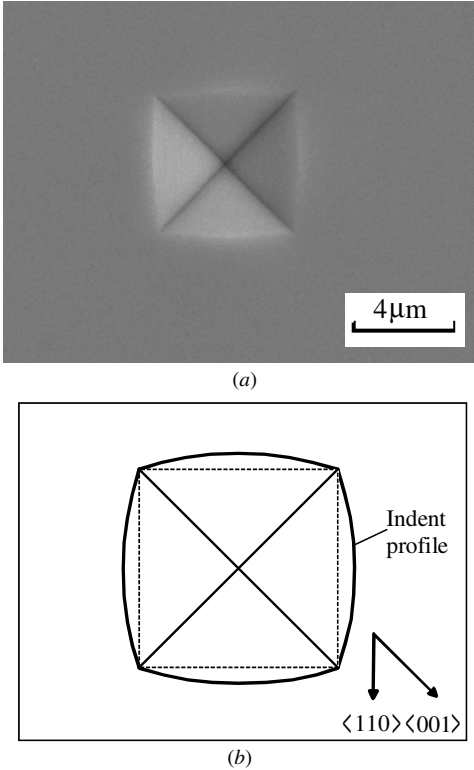


**Figure 5.** (a) SEM image and (b) schematic profile drawing of an indent obtained at a load of 150 mN with the Vickers indenter at a zero orientation angle.

### 3. Results and discussion

#### 3.1. Indent profile and microfracture

Figure 5(a) is an SEM image of an indent obtained at a load of 150 mN with the Vickers indenter at a zero-orientation angle (Vickers-0). Under this condition, the indent surface is very smooth and no fractures can be found on the surface. This demonstrates that although InP is a nominally brittle material, a completely ductile response can be obtained under suitable conditions. However, the shape of the indent is not square. The four margins of the indent have expanded outward, as schematized in figure 5(b). This phenomenon is presumably due to the anisotropy in elastic recovery of single-crystalline InP after unloading of the indenter. That is, the elastic recovery in the four  $\langle 100 \rangle$  directions is more significant than that in the  $\langle 110 \rangle$  directions. In other words, plastic deformation is more significant along  $\langle 110 \rangle$  than along  $\langle 100 \rangle$ . The anisotropic phenomenon in elastic recovery of material may cause microscopic undulations on the workpiece surface during machining if the workpiece rotates about the tool.

Figures 6(a) and (b) are SEM images of indents obtained at loads of 300 mN and 500 mN, respectively. Cracks have been generated around the indents. As the indentation load increases, the number and length of the cracks also increase. Most of the cracks are initiated near the corners of the indent and propagate radially. The paths of crack propagation are not straight and the propagation directions are somewhat random.

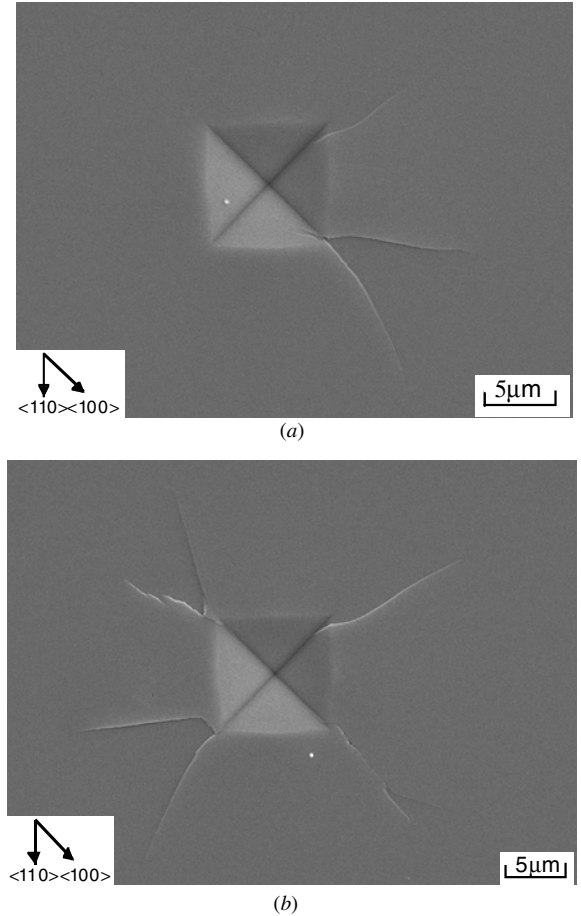


**Figure 6.** SEM images of Vickers indents obtained at (a) 300 mN and (b) 500 mN.

We can roughly divide the crack propagation directions into three kinds:  $\langle 100 \rangle$  directions,  $\langle 110 \rangle$  directions and directions between these two.

Figures 7(a) and (b) are SEM images of indents obtained using the same indenter but at an orientation angle of  $45^\circ$  (Vickers-45) at loads of 300 mN and 500 mN, respectively. At a load of 300 mN, only one radial crack is generated from the left corner of the indent along the  $\langle 110 \rangle$  direction. As the indentation load increases to 500 mN, more cracks appear at other corners. Compared to figure 6, the cracks in figure 7 are very straight and all are oriented along the  $\langle 110 \rangle$  directions. Another point worth noting is the indent profile. The four margins of the indent have been contracted inward, as schematized in figure 7(c). This phenomenon can also be explained by the anisotropy in elastic recovery. That is, elastic recovery in the  $\langle 100 \rangle$  directions is more significant than that in the  $\langle 110 \rangle$  directions.

Figures 8(a) and (b) are SEM images of indents generated by the spherical indenter at loads of 400 mN and 900 mN, respectively. Cracks have formed around the indent and propagated radially. As the indentation load increases, the number and length of cracks increased. Although the cracks have generally propagated in random directions, we can see that the majority are oriented along  $\langle 100 \rangle$ . From figure 8, it can also be seen that although the indenter

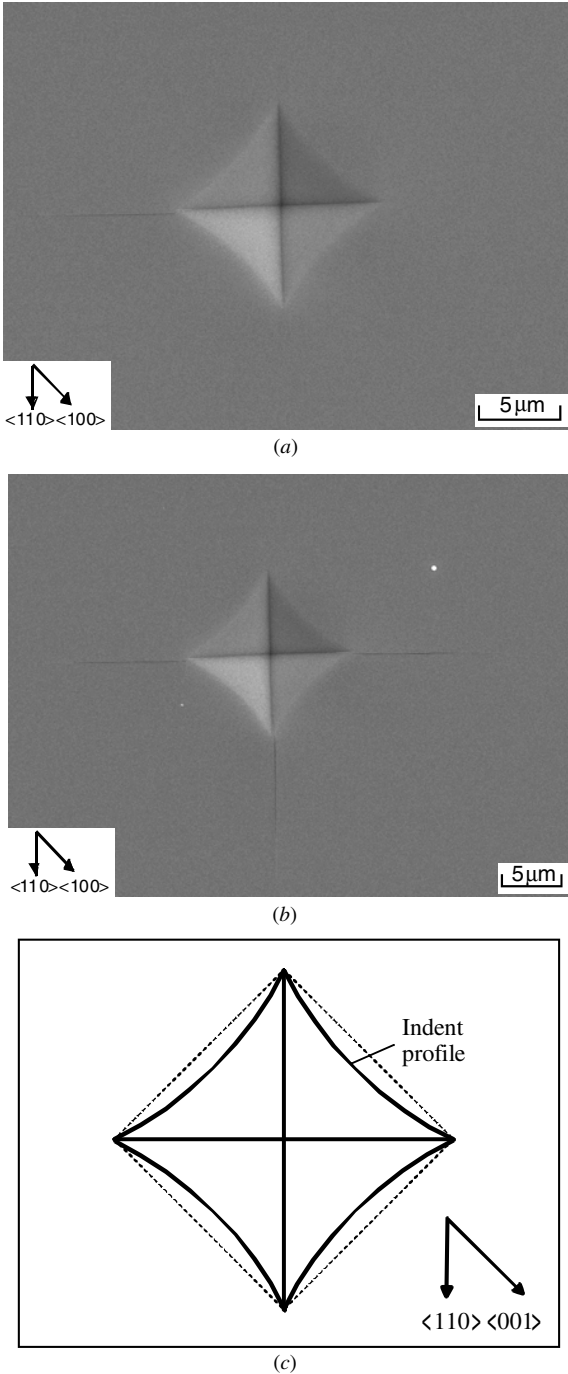


**Figure 7.** SEM images of indents obtained at loads of (a) 300 mN and (b) 500 mN; (c) is a schematic profile drawing of the indent.

is spherical, the residual indent is not round but almost quadrangular. This phenomenon is also caused by the anisotropy in elastic recovery. The asymmetry of the indent shown at the upper/lower sides in the photograph is caused by the geometrical error in the indenter head.

Figures 9 and 10 plot the average number of cracks and propagating directions versus the indentation load for the Vickers and spherical indenters, respectively. It can be seen that the critical indentation load for crack generation is 130 mN for Vickers-0, 160 mN for Vickers-45, and 200 mN for the spherical indenter. In figure 9(a), cracking behavior

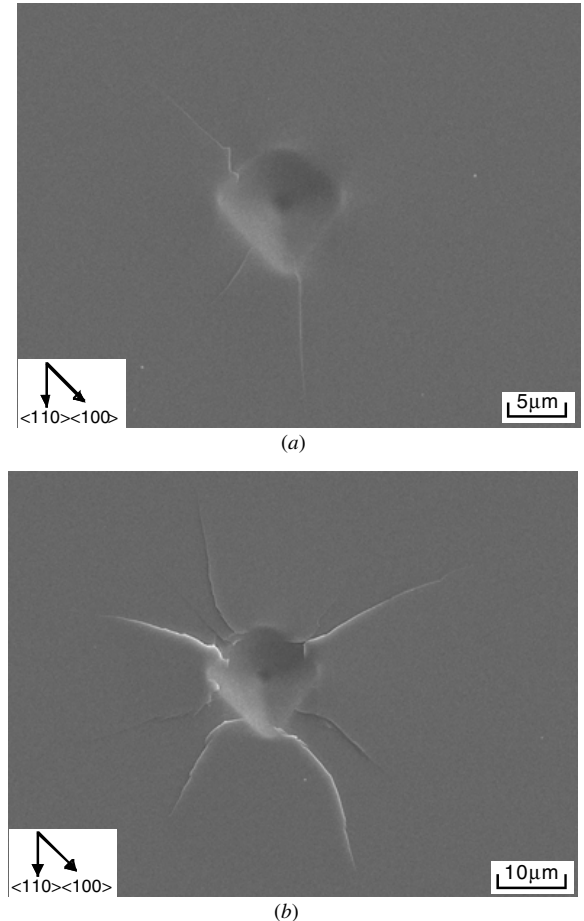


**Figure 8.** SEM images of indents generated by the spherical indenter at (a) 400 mN and (b) 900 mN.

is unstable when the load is in the range 130–200 mN, and the number of cracks increases sharply when the load is increased to 300 mN. The crack propagating direction is evenly distributed among  $\langle 100 \rangle$ ,  $\langle 110 \rangle$ , and directions between  $\langle 100 \rangle$  and  $\langle 110 \rangle$ . In figure 9(b), however, the number of cracks shows a gradual increase with load from 160 mN to 1000 mN, and most of the cracks are oriented in  $\langle 110 \rangle$  directions. The number of cracks increases at a significantly higher rate for the spherical indenter than for the Vickers indenter. Crack propagation is mainly along the  $\langle 100 \rangle$  direction for the spherical indenter.

On the basis of the above results, we can say that the deformation and microfracture of InP are strongly dependent on the geometry and orientation of the indenter. Compared to other directions,  $\langle 110 \rangle$  is more sensitive to the indenter ridge. If an indenter ridge is orientated along a  $\langle 110 \rangle$  direction, a crack readily forms along this direction under a small load before cracks along other directions are generated (figures 7, 9(b)). If the indenter ridge does not coincide with a  $\langle 110 \rangle$  direction (figures 6, 9(a)), or if a spherical indenter is used (figures 8, 10), cracks form under a higher load in a random manner, with  $\langle 100 \rangle$  as the primary cracking direction.

A comparison of the slopes of the plots in figures 9 and 10 reveals that the rate of increase of the number of cracks with indentation load is higher for the spherical indenter than

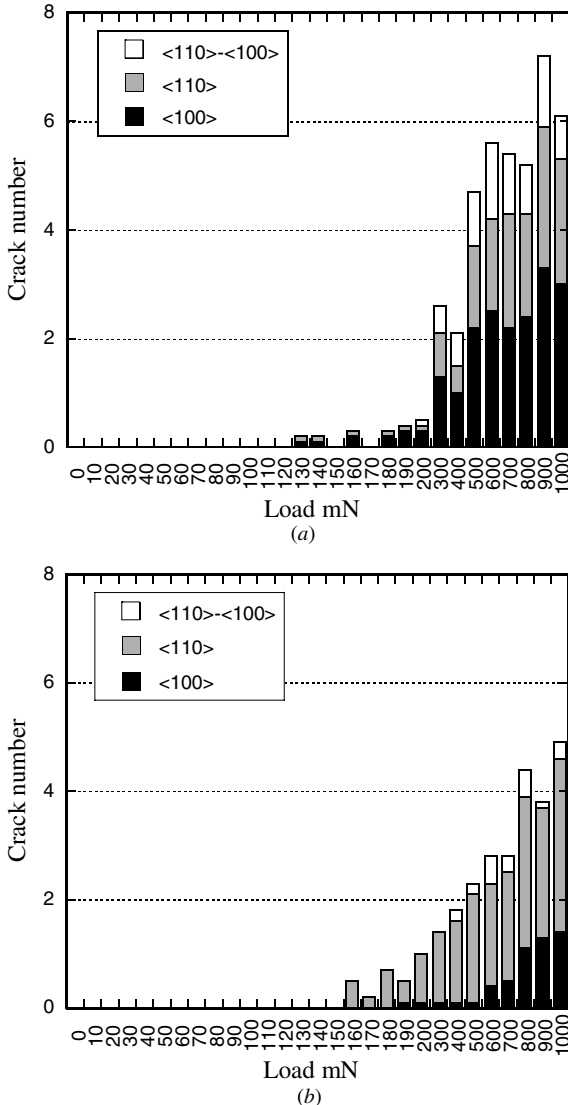


**Figure 9.** Plots of the average crack numbers and crack propagating directions against indentation load for the Vickers indenter at different orientation angles: (a)  $0^\circ$  and (b)  $45^\circ$ .

for the Vickers indenter. This may be explained in terms of the strain variation. Generally speaking, the effective strain in indentation is determined by the inclined angle between the indenter and sample surface. In the case of a Vickers pyramid, the inclined angle is constant, and hence the strain is constant regardless of depth. However, for a spherical indenter, the inclined angle of the indenter face increases as the indentation depth increases. The effective strain of a spherical indentation is proportional to  $a/R = \sin\beta$  ( $=\tan\beta$  if deformation is small) where  $a$  is the contact radius,  $R$  is the indenter radius and  $\beta$  is the inclination of the indenter face to the sample surface [21]. Thus, a spherical indentation with a progressively higher maximum load can produce a higher rate of increase of number of cracks than a Vickers indenter.

InP has a zinc-blende structure with a lattice constant of  $5.869 \text{ \AA}$ . As in the diamond-structure crystals silicon and germanium, the preferential slip systems are  $\langle 110 \rangle$  directions on  $\{111\}$  planes. However, unlike silicon and

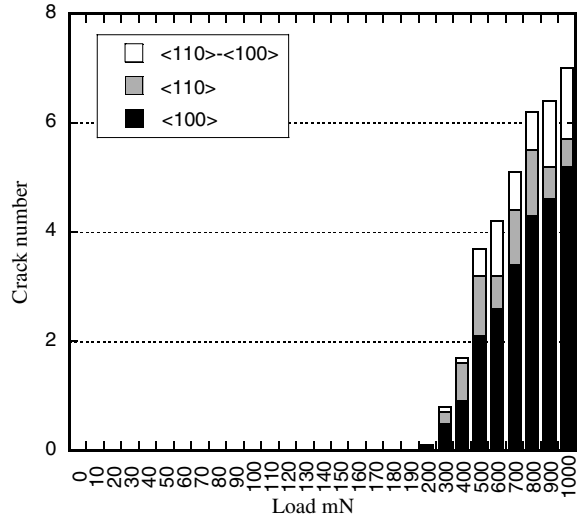


**Figure 10.** Plot of the average crack numbers and crack propagating directions against indentation load for the spherical indenter.

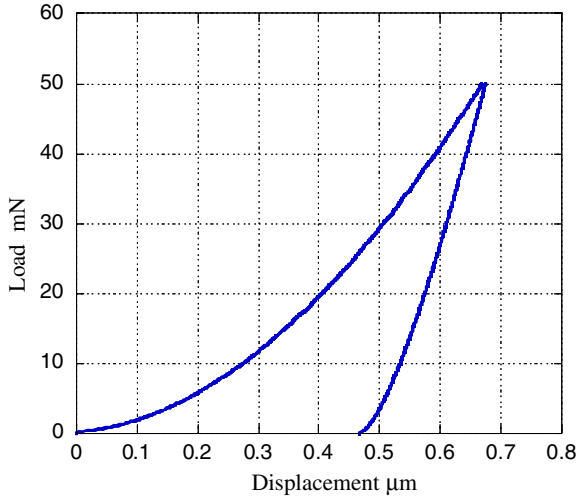
germanium whose preferential cleavage plane is also  $\{111\}$ , the preferential cleavage plane for InP is  $\{110\}$  [11]. The  $\langle 110 \rangle$  directions on the surface of the present experimental sample correspond simultaneously to the intersection lines between the  $\{111\}$  and  $\{100\}$  planes, and the intersection lines between the  $\{110\}$  planes and the  $\{100\}$  planes. Thus, the  $\langle 110 \rangle$  directions behave very uniquely. They are easy to deform plastically under shear stress conditions, while under tensile stress conditions, cracks are easily generated along this direction. It is the special crystallographic effects of the  $\langle 110 \rangle$  directions that have caused the changes of indent profile and crack propagation path seen in figures 5–10.

### 3.2. Load–displacement characteristics

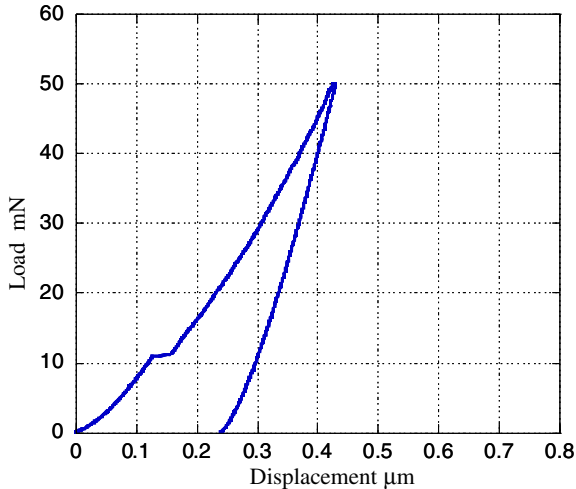
Figure 11 shows a typical load–displacement curve recorded during indentation with a Vickers indenter (orientation angle  $0^\circ$ ) at a maximum load of 50 mN. Unlike in silicon indentation, where distinct discontinuities in displacement (commonly referred to as ‘pop-outs’) are frequently observed during unloading [10, 22], in InP indentation, both the loading and unloading curves are smooth.

Figure 12 is a load–displacement curve obtained with a spherical indenter at the same maximum load (50 mN). As distinct from figure 11, there is a clear pop-in in the loading curve at a load of 12 mN, although the unloading curve remains smooth. After repeated testing, we found that even when we change the maximum indentation load the load at which the pop-ins occur (10–15 mN) remains roughly the same. Pop-in events have also been observed during the nanoindentation of InP and other materials, such as silicon, with spherical indenters [8, 23–26].

Some authors have regarded the pop-in phenomenon as a result of crack generation, or volume change caused by phase transformation of the indented material. In the present study, however, no crack was generated at a load of 10 mN. We also did not detect any phase transformations in InP beneath the indenter, as discussed in the following



**Figure 11.** Load–displacement curve recorded during indentation with a Vickers indenter at a maximum load of 50 mN.



**Figure 12.** Load–displacement curve obtained with a spherical indenter at a maximum load of 50 mN.

section. Thus, the pop-in in figure 12 is presumably caused by unstable dislocation activities (such as sudden slip nucleation or extension) in the indented material. As mentioned in section 3.1, for a spherical indenter, the effective strain increases with increasing indentation depth, while the strain of the Vickers indenter remains the same. As a result, pop-ins occur much more easily for spherical indenters. Another possible cause of pop-ins is the interfacial phenomena (such as stick-slip) between diamond and InP. For the same indentation depth, a spherical indenter induces a larger interface area than the Vickers indenter. Hence, pop-in events occurred in the case of the spherical indenter but not in the case of the Vickers indenter.

By comparing figures 11 and 12, we also found that for the Vickers indenter, the residual depth of the indent ( $0.47 \mu\text{m}$ ) was approximately 70% of the maximum indentation depth ( $0.67 \mu\text{m}$ ), whereas for the spherical indenter, the residual depth of the indent ( $0.24 \mu\text{m}$ ), the maximum indentation depth ( $0.43 \mu\text{m}$ ) and their ratio (56%) are all much smaller,

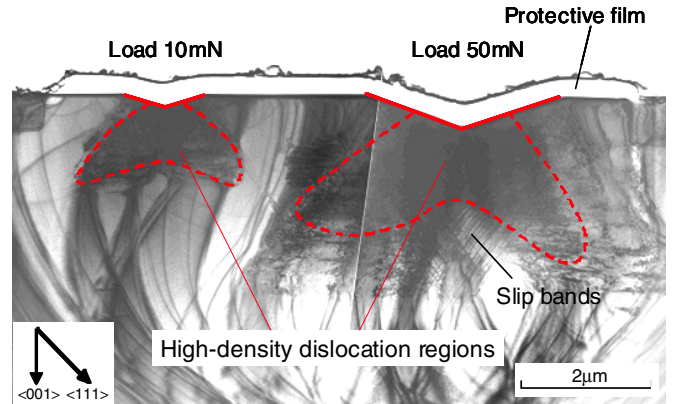


**Figure 13.** Cross-sectional TEM image of two indents obtained at 10 mN (left) and 50 mN (right).

even though the indentation load is the same. This indicates that a spherical indenter (a blunt cutting tool) causes more elastic deformation and less plastic deformation than a Vickers indenter (a sharp tool).

### 3.3. Subsurface damage

Figure 13 is a cross-sectional TEM image of two indents obtained at loads of 10 mN (left) and 50 mN (right). The long stripes seen across the whole image are the contrast caused by elastic bending of the TEM sample in FIB processing. No cracks can be found in the figure. Unlike silicon indentation [10, 27] where amorphous regions are generated below the indenters, there are no phase transformation regions in the bright-field image. For both indents, high-density dislocation regions (enclosed by the dotted lines) are formed beneath the indenters, extending downward. In these regions, dislocations generated on different slip planes interact intensively with each other to form sessile dislocations, which is a primary reason for work hardening. There is an obvious increase in the depth and area of the high-density dislocation region as the indentation load changes from 10 mN to 50 mN. Below the high-density dislocation region of the indent made at 50 mN, long slip bands are clearly visible. The slip bands are oriented at an angle of  $54^\circ$  to the sample surface ( $100$ ), demonstrating that slip deformation of InP occurs within the  $\{111\}$  planes, which are vertical to the TEM photograph plane, namely,  $(110)$ . Figure 13 also reveals a clearly ‘damage-free’ region between the two indents. Moreover, the distribution of dislocated region around either of the two indents is basically symmetrical to the indenter tip. Thus, we can conclude that there is still no interaction between neighboring indents at a distance of  $5 \mu\text{m}$ .

It is noteworthy that the dislocation distribution in figure 13 is distinctly different from those generated by spherical indenters [16], where long slip bands are predominant, rather than high-density dislocation regions. This indicates that compared to a blunt indenter, a sharp indenter causes more extensive plastic deformation in the material, thus leading to significant work hardening. However, for both types of indenters, the maximum depth of the

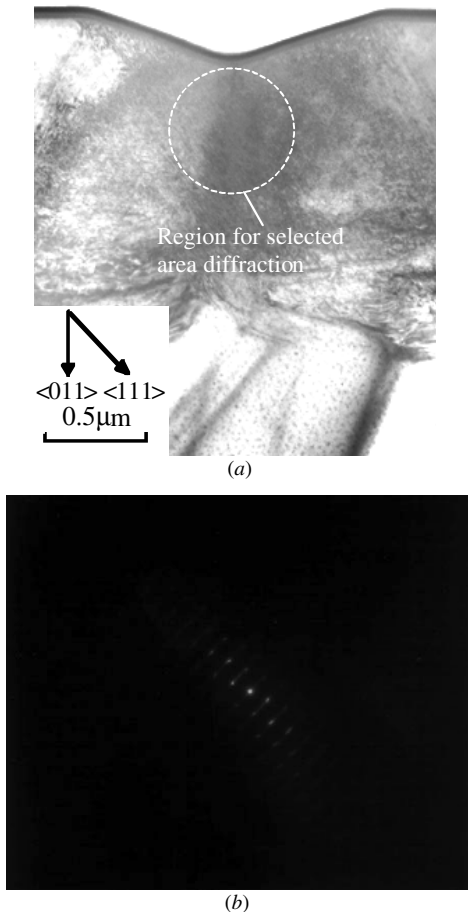


**Figure 14.** Selected area diffraction analysis results of the material below the indents obtained at 10 mN: (a) location of the selected area, (b) diffraction patterns.

dislocated region is by far (7–9 times) larger than the depth of the indent, indicating that in machining a very deep subsurface damage layer is generated that is far deeper than the depth of cut. Another important parameter is the critical load for ‘surface’ and ‘subsurface’ crack generation. From figures 9 and 10, we can see that the critical loads of ‘surface crack’ generation for all types of indenters are higher than 120 mN. However, Bradby *et al* [16] found that at a small load of 35 mN, ‘subsurface median cracks’ were generated under a spherical indenter. Although the present experimental conditions are not exactly the same as those of Bradby *et al*, we may presume that in brittle material indentations, ‘subsurface crack’ generation always precedes ‘surface crack’ generation.

Next, to confirm whether or not phase transformation occurred beneath the indenter, selected area diffraction analysis was performed. Figures 14(a) and (b) show the selected area location and the results, respectively, of electron diffraction analysis below the indent obtained at 10 mN. The diameter of the selected area diffraction spot is 500 nm. We do not observe any halo rings in figure 14(b), thus we can say that InP did not undergo amorphization. The diffraction pattern shows a zinc-blende lattice structure with an incident direction of  $\langle 1\ 1\ 0 \rangle$ . However, the diffraction spots are not round, but twisted and stretched, indicating that the crystalline periodicity has been severely disordered. Figure 15

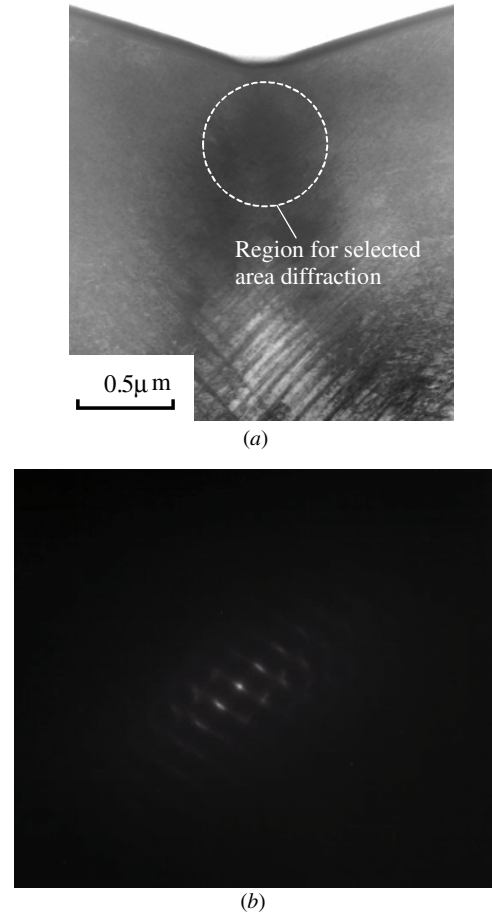


**Figure 15.** Selected area diffraction analysis results of the material below the indents obtained at 50 mN: (a) location of the selected area and (b) diffraction patterns.

shows the selected area location and the results of diffraction analysis below the indent obtained at 50 mN. The diffraction patterns are essentially the same as those shown in figure 14, except for a difference in the distorting direction of the diffraction spots caused by material rotation. It can also be seen that the distortion of diffraction spots in figure 15 is more significant than that in figure 14, demonstrating a load effect on plastic deformation intensity. From the above results, we can conclude that although significant plastic deformation takes place in the material beneath the indenter, no phase transformation occurs.

### 3.4. Stress distribution

Figure 16 shows the FEM-simulated residual stress distribution (von Mises stress) in the material beneath the indenter after unloading from a maximum load of 10 mN. Clearly, a high-stress region has been formed below the indenter, extending symmetrically towards the right and left. The shape of the high-stress region corresponds roughly to the high-density dislocation regions in the TEM images in figure 13. Beneath the two branches of the high-stress region, the stress gradation is very high, which might have caused the generation of long slip bands.

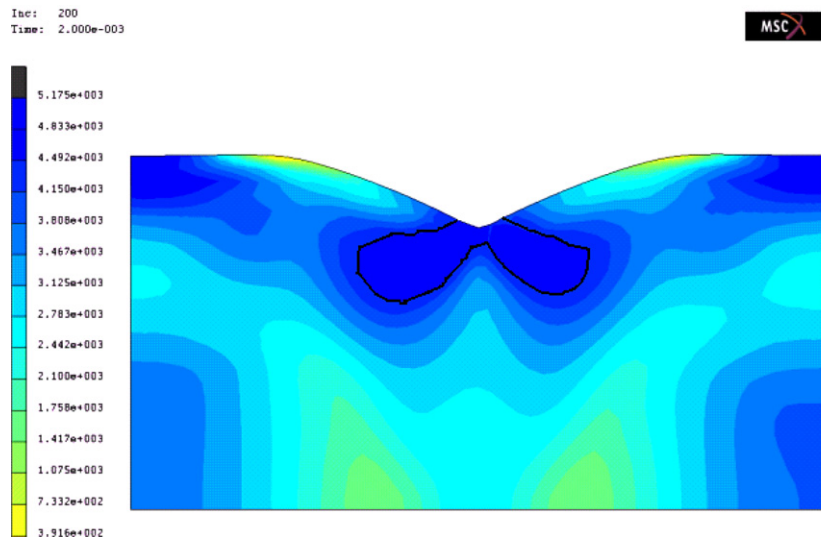


**Figure 16.** FEM-simulated distribution of von Mises stress in material below the Vickers indenter.

#### 4. Conclusion

Nanoindentation tests were performed on single-crystal InP under a wide range of loads with a sharp Vickers indenter and a spherical indenter. The main conclusions from this study can be summarized as follows:

- (1) Although InP is a nominally brittle material, a completely ductile response can be obtained at room temperature by performing indentation at a sufficiently small load. The critical indentation load for surface crack generation is 130–160 mN for the Vickers indenter and 200 mN for the spherical indenter.
- (2) Residual plastic deformation is significant along the  $\langle 1\bar{1}0 \rangle$  directions, while elastic recovery is significant along the  $\langle 100 \rangle$  directions. The anisotropy in elastic/plastic properties causes distinct changes in the shape of the indents.
- (3) Microcracking behavior of InP depends strongly on the indenter geometry and indenter-workpiece orientation. A spherical indenter causes more elastic deformation and less plastic deformation than a Vickers indenter.
- (4) Pop-in events occur during loading in the case of the spherical indenter, but not in the case of the Vickers indenter.
- (5) Dislocation-based plastic deformation dominates the nanoindentation of InP. A symmetrical high-density dislocation region is formed just beneath the indenter, below which a region with long slip bands is generated as indentation load increases. No phase transformation was detected.
- (6) In brittle material indentations, ‘subsurface cracks’ may occur at a lower load than ‘surface cracks’.
- (7) The shape and distribution of the FEM-simulated high-stress region correspond to the high-density dislocation regions beneath the indenter.

#### References

- [1] Pharr G M, Oliver W C and Harding D S 1991 New evidence for a pressure-induced phase transformation during the indentation of silicon *J. Mater. Res.* **6** 1129–30
- [2] Callahan D L and Morris J C 1992 The extent of phase transformation in silicon hardness indentations *J. Mater. Res.* **7** 1614–7
- [3] Kainer A, Gogotsi Y G and Nickel K G 1997 Phase transformations of silicon caused by contact loading *J. Appl. Phys.* **81** 3057–63
- [4] Clarke D R, Kroll M C, Kirchner P D and Cook R F 1988 Amorphization and conductivity of silicon and germanium induced by indentation *Phys. Rev. Lett.* **60** 2156–9
- [5] Bradby J E, Williams J S and Swain M V 2003 *In situ* electrical characterization of phase transformations in Si during indentation *Phys. Rev. B* **67** 085205
- [6] Saka H, Shimatani A, Sugamura M and Suprijad 2002 Transmission electron microscopy of amorphization and phase transition beneath indents in Si *Phil. Mag. A* **82** 1971–81
- [7] Zarudi I, Zou J and Zhang L C 2003 Microstructures of phases in indented silicon: a high resolution characterization *Appl. Phys. Lett.* **82** 874–6
- [8] Juliano T, Domnich V and Gogotsi Y 2004 Examining pressure-induced phase transformations in silicon by spherical indentation and Raman spectroscopy: a statistical study *J. Mater. Res.* **19** 3099
- [9] Jang J, Lance M J, Wen S, Tsui T Y and Pharr G M 2005 Indentation-induced phase transformations in silicon: influences of load, rate and indenter angle on the transformation behavior *Acta Mater.* **53** 1759–70
- [10] Yan J, Takahashi H, Gai X, Harada H, Tamaki J and Kuriyagawa T 2006 Load effects on the phase transformation of single-crystal silicon during nanoindentation tests *Mater. Sci. Eng. A* **423** 19–23
- [11] Brasen D 1976 Hardness anisotropy of InP *J. Mater. Sci.* **11** 791–3
- [12] Bourhis E L, Riviere J P and Zozime A 1996 Material flow under an indenter in indium phosphide *J. Mater. Sci.* **31** 6571–6
- [13] Yonenaga I and Suzuki T 2002 Indentation hardnesses of semiconductors and a scaling rule *Phil. Mag. Lett.* **82** 535–42

- [14] Bradby J E, Williams J S, Swain M V and Munroe P 2004 Pop-in events induced by spherical indentation in compound semiconductors *J. Mater. Res.* **19** 380–6
- [15] Bradby J E, Williams J S and Wong-Leung J 2002 Spherical indentation of compound semiconductors *Phil. Mag. A* **82** 1931–9
- [16] Bradby J E, Williams J S, Wong-Leung J, Swain M V and Munroe P 2001 Mechanical deformation of InP and GaAs by spherical indentation *Appl. Phys. Lett.* **78** 3235–7
- [17] Yan J, Yoshino M, Kuriyagawa T, Shirakashi T, Syoji K and Komanduri R 2001 On the ductile machining of silicon for micro electro-mechanical systems (MEMS), opto-electronic and optical applications *Mater. Sci. Eng. A* **297** 230–4
- [18] Yan J, Syoji K, Kuriyagawa T and Suzuki H 2002 Ductile regime turning at large tool feed *J. Mater. Process. Technol.* **121** 363–72
- [19] Rats D, Vandenbulcke L, Boher C and Farges G 1997 Tribological study of diamond coatings on titanium alloys *Surf. Coat. Technol.* **94–5** 555–60
- [20] Hayward I P, Singer I L and Seitzman L E 1992 Effect of roughness on the friction of diamond on CVD diamond coatings *Wear* **157** 215–27
- [21] Johnson K L 1987 *Contact Mechanics* (Cambridge: Cambridge University Press)
- [22] Yan J, Takahashi H, Tamaki J, Gai X, Harada H and Patten J 2005 Nanoindentation tests on diamond-machined silicon wafers *Appl. Phys. Lett.* **86** 181913
- [23] Bradby J E, Williams J S, Wong-Leung J, Swain M V and Munroe P 2000 Transmission electron microscopy observation of deformation microstructure under spherical indentation in silicon *Appl. Phys. Lett.* **77** 3749
- [24] Brady J E, Williams J S, Wong-Leung J, Swain M V and Munroe P 2001 Mechanical deformation in silicon by micro-indentation *J. Mater. Res.* **16** 1500–7
- [25] Leipner H S, Lorenz D, Zeckzer A, Lei H and Grau P 2001 Nanoindentation pop-in effect in semiconductors *Physica B* **446** 308–10
- [26] Lorenz D, Zeckzer A, Hilpert U, Grau P, Johansen H and Leipner H S 2003 Pop-in effect as homogeneous nucleation of dislocations during nanoindentation *Phys. Rev. B* **67** 172101
- [27] Yan J, Takahashi H, Tamaki J, Gai X and Kuriyagawa T 2005 Transmission electron microscopic observation of nanoindentations made on ductile-machined silicon wafers *Appl. Phys. Lett.* **87** 211901